GEOCHEMISTRY

The evolution of Earth's surficial Mg cycle over the past 2 billion years

Zhiguang Xia[1,2,3,4]†, Shilei Li[2,5]†, Zhongya Hu[1,6], Or Bialik[7], Tianyu Chen[1,2], Mebrahtu F. Weldeghebriel[8,9], Qishun Fan[10], Junxuan Fan[1], Xiangdong Wang[1], Shichao An[1,2], Feifei Zhang[1], Haoran Xu[1,2], Jiayang Chen[1,2], Zhihan Ji[1,2], Shuzhong Shen[1], Tim K. Lowenstein[8]*, Weiqiang Li[1,2]*

The surficial cycling of Mg is coupled with the global carbon cycle, a predominant control of Earth's climate. However, how Earth's surficial Mg cycle evolved with time has been elusive. Magnesium isotope signatures of seawater ($\delta^{26}Mg_{sw}$) track the surficial Mg cycle, which could provide crucial information on the carbon cycle in Earth's history. Here, we present a reconstruction of $\delta^{26}Mg_{sw}$ evolution over the past 2 billion years using marine halite fluid inclusions and sedimentary dolostones. The data show that $\delta^{26}Mg_{sw}$ decreased, with fluctuations, by about 1.4‰ from the Paleoproterozoic to the present time. Mass balance calculations based on this $\delta^{26}Mg_{sw}$ record reveal a long-term decline in net dolostone burial (NDB) over the past 2 billion years, due to the decrease in dolomitization in the oceans and the increase in dolostone weathering on the continents. This underlines a previously underappreciated connection between the weathering-burial cycle of dolostone and the Earth's climate on geologic timescales.

INTRODUCTION

Key external forcings of Earth's climate, including solar luminosity, mantle outgassing intensity, and the composition and exposure of crustal rocks, have changed remarkably and irreversibly over geological time (*1*). Despite that, the Earth's surficial temperature has remained within the habitable range for most of its history, which is believed to be regulated by atmospheric CO_2 levels through negative feedback in the carbonate-silicate cycles (*2*, *3*). However, the exact mechanisms remain highly debated; some invoke weathering of silicates on continents (*3*, *4*), whereas others emphasize reverse weathering on seafloors (*5*, *6*). Addressing such problems requires the acquisition and interpretation of various secular records of different key elements for surficial processes both on land and in the oceans.

The surficial Mg cycle is interconnected by various processes, including continental weathering, high- and low-temperature alteration of oceanic crust, and formation of carbonates and clays on the seafloor. Through these interactions, the Mg cycle closely interacts with the geochemical cycles of carbon, calcium, and silicon (*7*–*9*). Despite its relevance to Earth's habitability, quantitative studies of ancient surficial Mg cycles are challenging, particularly for the Precambrian periods (*10*). Previous attempts to reconstruct Mg cycles based on the compiled volume of sedimentary dolostones over geologic time (*9*) were hampered by the uneven preservation of carbonate rocks deposited in different environments and incomplete data for compilation, which worsened markedly for older records (*11*). Another record of Mg cycling is the Mg concentration in ancient seawater, recovered from fluid inclusions in halite (*12*), although the data are mainly restricted to the Phanerozoic Eon.

Magnesium isotopes are an effective tracer for surficial Mg cycles. Magnesium in the oceans is supplied from the weathering of silicates and Mg-bearing carbonates (mainly dolomite), which have a large difference in Mg isotope ratios [expressed in delta notation: $\delta^{26}Mg = (R_{sample}/R_{standard} - 1) \times 1000$, $R = {}^{26}Mg/{}^{24}Mg$, the standard is DSM3]. The majority of igneous silicate rocks have similar $\delta^{26}Mg$ values that cluster around -0.25 ± 0.07‰, whereas carbonates have much lower values of $\delta^{26}Mg$, commonly between -1 and -5‰ dependent on mineralogy, temperature, and precipitation kinetics (*13*). Thus, changes in the relative contribution of carbonate to silicate sources could lead to different Mg isotope compositions of Mg input into the oceans (*14*). Mg is removed from seawater via the formation of Mg-bearing carbonates and Mg-bearing silicates. Precipitation of dolomite and magnesian calcite [distinguished as high-Mg calcite and low-Mg calcite at a composition above and below 4 mol % $MgCO_3$ (*15*)] at ambient temperatures is associated with a fractionation factor ($\Delta^{26}Mg_{min\text{-}aq} = \delta^{26}Mg_{mineral} - \delta^{26}Mg_{aqueous}$) of ~−2‰ or lower (*16*, *17*), whereas uptake of aqueous Mg into silicates is generally associated with positive to zero $\Delta^{26}Mg_{min\text{-}aq}$ fractionation, depending on reaction temperature and mineralogy (*13*, *14*). Consequently, a change in the relative contribution of the carbonate Mg sink relative to the silicate sink would also change the isotopic ratio of seawater Mg (*8*, *16*). Therefore, Mg isotopes in seawater respond to changes in the balance between silicates and carbonates of the surficial Mg cycles, on both the source and sink sides. The geologic record of seawater $\delta^{26}Mg$ can thus be used to interrogate the long-term global carbonate-silicate cycles.

[1]State Key Laboratory for Mineral Deposits Research, School of Earth Sciences and Engineering, Nanjing University, Nanjing 210023, Jiangsu, China. [2]Frontiers Science Center for Critical Earth Material Cycling, Nanjing University, Nanjing 210023, Jiangsu, China. [3]State Key Laboratory of Oil and Gas Reservoir Geology and Exploitation & Institute of Sedimentary Geology, Chengdu University of Technology, Chengdu 610059, China. [4]International Center for Sedimentary Geochemistry and Biogeochemistry Research, Chengdu University of Technology, Chengdu 610059, China. [5]Key Laboratory of Surficial Geochemistry, Ministry of Education, School of Earth Sciences, Nanjing University, Nanjing 210023, China. [6]State Key Laboratory of Marine Geology, School of Ocean and Earth Science, Tongji University, Shanghai 200092, China. [7]Institute of Geology and Palaeontology, University of Muenster, Corrensstr. 24, 48149 Münster, Germany. [8]Department of Earth Sciences, Binghamton University, NY 13902, USA. [9]Department of Geosciences, Princeton University, NJ 08544, USA. [10]Key Laboratory of Comprehensive and Highly Efficient Utilization of Salt Lake Resources, Qinghai Provincial Key Laboratory of Geology and Environment of Salt Lakes, Qinghai Institute of Salt Lakes, Chinese Academy of Sciences, Xining 810008, China.
*Corresponding author. Email: lowenst@binghamton.edu (T.K.L.); liweiqiang@nju.edu.cn (W.L.)
†These author contributed equally to this work.

Several studies reconstructed the Mg isotope composition of seawater during the Cenozoic using biogenic calcite or aragonite (*8*, *18*). Calcite and aragonite, however, are susceptible to diagenesis, thus their fidelity as Mg isotope archives for older geological times may require additional constraints (such as Ca isotopes) for verification (*19*). In contrast, Mg isotopes in dolomite have proven to be resistant to various postdepositional overprinting processes (*20*, *21*). Dolostones are abundant in ancient marine sedimentary sequences, and the Mg isotope fractionation between dolomite and aqueous solution is well-constrained (*16*, *17*). These features provide an opportunity to reconstruct the Mg isotope composition of ancient seawater. An alternative seawater Mg isotope archive is marine halite. Bedded halite from marine evaporites contains primary fluid inclusions, which preserve the Mg isotope composition of contemporaneous seawater (*22*). The advantage of halite is that seawater δ^{26}Mg values can be directly measured from fluid inclusions without the application of Mg isotope fractionation factors, because the precipitation of halite from evaporating seawater occurs before the precipitation of Mg-bearing evaporite minerals (*22*). Both the dolomite and halite records have certain limitations as seawater δ^{26}Mg archives, thus data screening is necessary. In practice, however, as shown in the following sections, the two records complement each other and place strong constraints on seawater δ^{26}Mg.

In this study, we use Mg isotopes measured in marine dolostone and halite to generate a record of Mg isotope composition of seawater ($\delta^{26}Mg_{sw}$) for the past 2 billion years. We compile a comprehensive Mg isotope dataset for marine sedimentary dolomite over the past 2 billion years, including 1809 analyses from 58 lithostratigraphic units reported in the literature and 425 additional analyses from 25 lithostratigraphic units in this study (Supplementary Materials, tables S1 and S2, and fig. S1). For the Phanerozoic, 103 marine halite samples from 37 lithostratigraphic units are also compiled, including 84 additional analyses from 29 lithostratigraphic units (Supplementary Materials and table S3). Halite samples are carefully selected based on geological and textural criteria to ensure that the fluid inclusions are primary and contain evaporated seawater (Supplementary Materials and fig. S2). In addition, only halites with $^{87}Sr/^{86}Sr$ ratios consistent with coeval seawater are included (Supplementary Materials and fig. S3). Non-seawater $^{87}Sr/^{86}Sr$ ratios in halite indicate notable contributions of non-marine waters to the enclosed evaporite basin, which could alter the seawater Mg isotope composition of the brine.

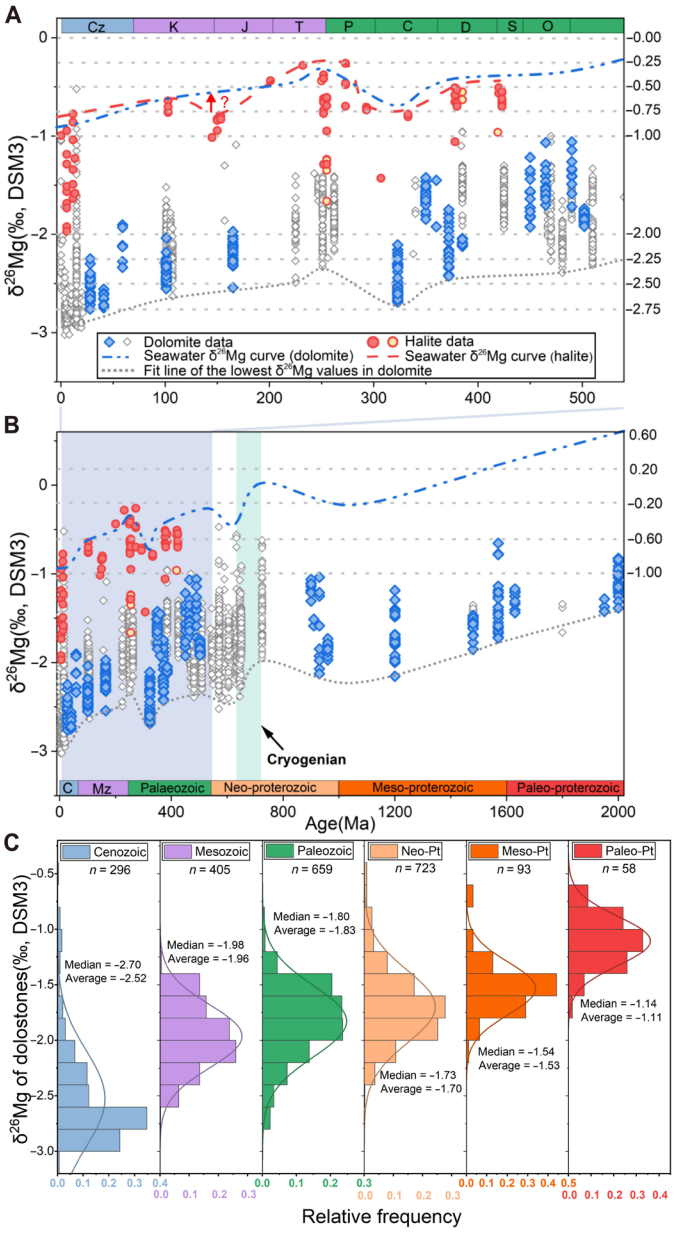

Fig. 1. Summary of Mg isotope data from sedimentary archives. (**A**) Mg isotope data from Phanerozoic dolostone and halite. Blue diamonds denote additional data for dolostones in this study, and open diamonds denote published data for dolostones. Red-filled circles denote additional data for halite in this study, and yellow-filled circles are published halite Mg isotope data. Dashed blue and red lines denote the reconstructed $\delta^{26}Mg_{sw}$ curves based on dolostones and halites, respectively. The dotted gray line shows the lower contour for the dolostone records. (**B**) Mg isotope records from dolostone and halite over the past 2 billion years. Legends are the same as in plot (A). (**C**) Histogram of δ^{26}Mg for dolostone over six geologic time intervals of the past 2 billion years.

RESULTS

Seawater Mg isotope composition in the past 2 billion years

Marine dolostone samples show large variations in δ^{26}Mg values (−3.02 to −0.47‰) over the past 2 billion years (Fig. 1, A and B). However, histograms of data for six major geological time brackets show continuous decreases in the median, average, and overall range of dolostone δ^{26}Mg values through the Paleoproterozoic, Mesoproterozoic, Neoproterozoic, Paleozoic, Mesozoic, and Cenozoic (Fig. 1C). The Mg isotope variability of dolostones within a sedimentary unit mainly stemmed from the dolomitization processes (*23*, *24*). Isotopic evolution of Mg in dolomitization fluids can occur along a diffusion/advection profile on a scale of meters to hundreds of meters (*17*, *25*, *26*) or across a carbonate platform on a scale of hundreds of kilometers (Supplementary Materials and figs. S4 and S5) or even within an enclosed basin on the continental scale (*19*, *27*). Nonetheless, dolomitization invariably removes light Mg isotopes from the fluid, elevating the δ^{26}Mg value of the remaining fluid and the δ^{26}Mg values of dolomite precipitated from that fluid (*23*, *24*). Therefore, δ^{26}Mg values of marine dolostones tend to be higher than the seawater-equilibrated δ^{26}Mg value, and the lowest δ^{26}Mg values of syn-depositional dolostones have the

greatest possibility of approaching the seawater-equilibrated $\delta^{26}Mg$ values (*19*, *28*).

To establish a curve of $\delta^{26}Mg_{sw}$ through time, a contour is extended between the lowest $\delta^{26}Mg$ values (hinge points) of the dolomite dataset in each time slice. We then apply a + 2‰ offset (i.e., the Mg isotope fractionation factor between dolomite and seawater) to the contour (Fig. 1). Data points that are abruptly higher than the neighboring hinge points may be caused by basin restriction effects. Such points are excluded because abrupt changes in $\delta^{26}Mg_{sw}$ are unlikely considering the long residence time of Mg in the oceans (i.e., ~10 million years presently). Small sample sets with $n < 10$ are not used to define the contour because they may not be representative of that period. The goal is to reconstruct long-term variations of $\delta^{26}Mg_{sw}$ but not sub-million-year scale perturbations of $\delta^{26}Mg_{sw}$. The $n = 10$ threshold also ensures that the majority (i.e., > 50%) of our subdatasets of dolostones can be used for establishing the $\delta^{26}Mg_{sw}$ record for the past 2 billion years (fig. S6B).

A second seawater Mg isotope archive, fluid inclusions in marine halite, is available for the Phanerozoic. Marine halites also exhibit variability in $\delta^{26}Mg$ values (−1.97 to 0.06‰; Fig. 1, A and B). This is because the bulk dissolution of halite is used for Mg isotope analysis of fluid inclusions. Measured $\delta^{26}Mg$ values are therefore complicated by possible soluble Mg-bearing evaporite mineral inclusions. For example, for the Late Miocene halite from Egypt, the measured $\delta^{26}Mg$ values vary from −1.63 to −0.78‰. These samples show a negative correlation between bulk Mg and K concentrations and $\delta^{26}Mg$ values (Supplementary Materials and fig. S7), indicating mixing of fluid inclusions and ^{24}Mg-enriched mineral inclusions. Detailed scanning electron microscopy (SEM) imaging confirms that polyhalite occurs in some halite samples (Supplementary Materials and fig. S8). Polyhalite is known to be enriched in light Mg isotopes (*22*). Note that although the entrapment of polyhalite could lower the measured $\delta^{26}Mg$ of bulk halite, this cannot alter the Mg isotope composition of evolved seawater during earlier stages of halite precipitation and brine evaporation, as has been quantified by thermodynamic simulation and isotope mass balance calculations (Supplementary Materials and fig. S9). To summarize, the $\delta^{26}Mg$ value measured from marine halite could be lower than contemporaneous seawater, and the highest $\delta^{26}Mg$ values from marine halite of a particular age can be used to define the lower boundary of the $\delta^{26}Mg_{sw}$ curve.

The dolomite-based $\delta^{26}Mg_{sw}$ curve is consistent with the upper contour of the halite-based $\delta^{26}Mg_{sw}$ curve within 0.2‰ for the Phanerozoic Eon (Fig. 1A). This consistency is crucial because marine dolostone and halite are totally independent seawater Mg isotope archives, and they are complementary as the dolomite-based $\delta^{26}Mg_{sw}$ value could be higher than the actual $\delta^{26}Mg_{sw}$, whereas the halite-based $\delta^{26}Mg_{sw}$ could be lower than the actual $\delta^{26}Mg_{sw}$. The reconstructed $\delta^{26}Mg_{sw}$ is around −0.8‰ in the Cenozoic, consistent with previous studies (*8*, *18*). The $\delta^{26}Mg_{sw}$ increases with increasing age in the Mesozoic and reaches the peak Phanerozoic value, −0.3‰, around the Permian-Triassic boundary. The $\delta^{26}Mg_{sw}$ decreases to ~−0.7‰ during the Carboniferous and increases with age to ~−0.2‰ in the Cambrian.

The dolomite-based $\delta^{26}Mg_{sw}$ curve shows pronounced fluctuations in the Neoproterozoic that coincide with extreme climatic events such as the freezing and melting of Snowball Earth (*29*). The hinge points for the $\delta^{26}Mg_{sw}$ curve are sparser in the Proterozoic, particularly before 800 Ma, but they reveal an increasing trend of $\delta^{26}Mg_{sw}$ with increasing age, from −0.2 ± 0.2‰ during the Neoproterozoic, to 0 ± 0.2‰ during the Mesoproterozoic, to ≥ +0.5‰ in the early Paleoproterozoic (Fig. 1B). Considering that Earth was in the "Boring Billion" period between 800 and 1800 Ma marked by the lack of large sediment C isotope excursions (*30*) and orogenic quiescence (*31*), no marked perturbations in the surficial Mg cycle are expected to occur during this period. If so, the Monte Carlo modeling results show that the number of hinge points ($n = 7$) is sufficient to capture the trend of the $\delta^{26}Mg_{sw}$ curve during the Mesoproterozoic and early Paleoproterozoic (fig. S10). Additional Mg isotope data in the future will further refine the $\delta^{26}Mg_{sw}$ curve for the Proterozoic.

Overall, by combining two large Mg isotope datasets of dolomite and halite, we show that the Mg isotope composition of seawater changed notably during the past 2 billion years. The $\delta^{26}Mg_{sw}$ decreased from >+0.5‰ in the early Paleoproterozoic to a modern value of −0.8‰, with fluctuations during the Neoproterozoic and Paleozoic-Mesozoic transition. The present $\delta^{26}Mg_{sw}$ curve has limited temporal resolution (Fig. 1, A and B), and it is possible that finer-scale fluctuations in $\delta^{26}Mg_{sw}$ could be revealed with more data. Such refinement, however, is unlikely to change the overall statistical pattern of decreasing dolostone $\delta^{26}Mg$ in successively younger geological ages (Fig. 1C). The first-order observation, that the $\delta^{26}Mg_{sw}$ decreased by ~1.4‰ in the past 2 billion years, underlines fundamental changes in Earth's surficial Mg cycles with time.

Secular changes in surficial Mg cycles constrained from $\delta^{26}Mg_{sw}$

On the basis of the $\delta^{26}Mg_{sw}$ record, we next quantify how the surficial Mg cycle evolved over the past 2 billion years with a mass balance model. As described in the introductory paragraphs, the surficial Mg cycle is controlled by carbonate and silicate weathering expressed as riverine input to the ocean (*14*) and Mg removal as either carbonate minerals via dolomitization or silicate minerals through marine clay formation and alteration of oceanic crust (*9*, *14*, *32*). Note that when carbonate burial exceeds carbonate weathering, the excess carbonate burial would consume the alkalinity generated by silicate weathering and consequently remove CO_2 from the Earth's surface (*3*, *4*). Therefore, the imbalances between weathering and burial of Mg carbonates could induce net surficial carbon fluxes that might affect the Earth's climate system. Thus, our model is particularly focused on calculating variations in the imbalances between Mg carbonate weathering and burial.

The mathematical framework of the model is based on elemental and isotopic mass balance equations, an approach that has proven effective for studies of elements with long-residence times in seawater (*8*, *33*, *34*)

$$F_{\text{carb-in}} + F_{\text{sili-in}} = F_{\text{carb-out}} + F_{\text{sili-out}} \quad (1)$$

$$\delta_{\text{carb-in}}F_{\text{carb-in}} + \delta_{\text{sili-in}}F_{\text{sili-in}} = \delta_{\text{carb-out}}F_{\text{carb-out}} + \delta_{\text{sili-out}}F_{\text{sili-out}} \quad (2)$$

where F and δ represent the fluxes and isotopic compositions of Mg for the silicates (subscript: $_{\text{sili}}$) and carbonates (subscript: $_{\text{carb}}$) as influx (subscript: $_{\text{-in}}$) and outflux (subscript: $_{\text{-out}}$).

The above equations can be solved using a stochastic modeling approach. In the modeling, all the possible values for each F and δ parameter in the above equations are searched and tested by the Monte Carlo method. The fraction of each individual flux relative to the total Mg flux is first allowed to vary between 0 and 1 in the model calculation. For Mg isotope compositions of the influxes and

outfluxes of carbonates ($\delta_{carb\text{-}in}$ and $\delta_{carb\text{-}out}$) and silicates ($\delta_{sili\text{-}in}$ and $\delta_{sili\text{-}out}$), estimates with realistic 2 sigma (95% confidence level) uncertainties under normal distribution are ascribed. Specifically, we note that the Mg isotope compositions of the outfluxes are controlled by the Mg isotope composition of seawater and the Mg isotope fractionation factors associated with carbonate precipitation and secondary silicate formation (i.e., $\delta_{carb\text{-}out} = \delta_{sw} - \Delta_{carb\text{-}sw}$, $\delta_{sili\text{-}out} = \delta_{sw} - \Delta_{sili\text{-}sw}$). δ_{sw} is reconstructed in this study, whereas $\Delta_{carb\text{-}sw}$ and $\Delta_{sili\text{-}sw}$ factors are provided in the literature. Details of the parameter settings for the mass balance equations and Monte Carlo modeling algorithms are provided in Materials and Methods and the Supplementary Materials.

We first numerically solve the elemental and isotopic mass balance equations for the modern Mg cycle ($\delta^{26}Mg_{sw} = -0.8‰$). Infinite solutions of Mg influx and Mg outflux values for silicates and Mg carbonates (predominantly dolostones) exist (red dots in Fig. 2). However, these solutions define a broad linear trend in a cross plot of $F_{carb\text{-}in}/F_{Total\text{-}in}$ versus $F_{carb\text{-}out}/F_{Total\text{-}out}$ for each given $\delta^{26}Mg_{sw}$ value, regardless of the freedom in flux values (Fig. 2). In reality, $F_{carb\text{-}in}/F_{Total\text{-}in}$ should have a much more restricted range. The contribution of silicate weathering to riverine input of Mg was estimated in several studies, which yielded a range of 0.41 to 0.52 (see Materials and Methods). When we further take the contribution of submarine weathering of silicates into consideration, the actual $F_{carb\text{-}in}/F_{total\text{-}in}$ ratio for modern seawater is estimated to be 0.42 ± 0.08 (2σ). The Monte Carlo calculation results for such a distribution of $F_{carb\text{-}in}/F_{Total\text{-}in}$ are shown by colored red contours in Fig. 2, and the corresponding $F_{carb\text{-}out}/F_{total\text{-}out}$ is constrained to be 0.39 ± 0.26 (2σ, red histogram on the right side of Fig. 2), which agrees with the modern $F_{carb\text{-}out}/F_{total\text{-}out}$ (0.27 to 0.52) estimated recently (*35*).

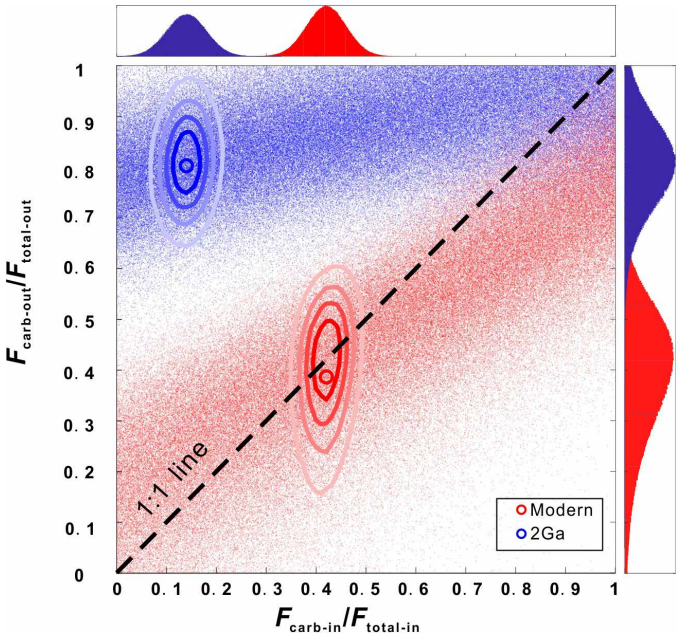

Fig. 2. Monte Carlo modeling results for global Mg cycles in the modern and the Paleoproterozoic. Red and blue dots represent solutions of elemental and isotopic mass balance equations for a $\delta^{26}Mg_{sw}$ value of −0.8‰ (i.e., modern seawater) and + 0.6‰ (i.e., Paleoproterozoic seawater), respectively. For these solutions, $F_{carb\text{-}in}/F_{Total\text{-}in}$ is allowed to vary between 0 and 1. However, in reality, $F_{carb\text{-}in}/F_{Total\text{-}in}$ should have a limited range. A more realistic range of $F_{carb\text{-}in}/F_{Total\text{-}in}$ is further defined by a normal distribution, and the corresponding $F_{carb\text{-}out}/F_{Total\text{-}out}$ could be calculated accordingly (for details, see Materials and Methods). These refined ranges are shown as graded color contours in the main plots and histograms on the side plots. The red and blue circles are the average values of recalculated $F_{carb\text{-}in}/F_{Total\text{-}in}$ and $F_{carb\text{-}out}/F_{Total\text{-}out}$ ratios in the modern and Paleoproterozoic, respectively.

The same Monte Carlo method is applied to Paleoproterozoic seawater that has a $\delta^{26}Mg_{sw}$ value of 0.6‰; the numerical solutions are shown as blue dots in Fig. 2. The modeling results predominantly plot above the 1:1 line and show that $F_{carb\text{-}out}/F_{total\text{-}out}$ was markedly greater than $F_{carb\text{-}in}/F_{total\text{-}in}$ in seawater at 2000 Ma. This means that in the Paleoproterozoic, dolostone burial was higher than dolostone weathering flux. To quantify this imbalance in Mg surficial cycling, we define a parameter, Net Dolostone Burial (NDB), that represents the difference between the proportion of Mg removed by dolostone formation in total Mg outflux and the proportion of Mg supplied by dolostone weathering in total Mg influx (i.e., $NDB = F_{carb\text{-}out}/F_{total\text{-}out} - F_{carb\text{-}in}/F_{total\text{-}in}$). On the basis of the modeling results shown in Fig. 2, the NDB is estimated at 0.66 ± 0.19 (2σ). By contrast, modern oceans are in an approximate balance between $F_{carb\text{-}out}/F_{total\text{-}out}$ and $F_{carb\text{-}in}/F_{total\text{-}in}$, with NDB ranging from −0.16 to 0.09, as the data points in the contoured area are close to the 1:1 line on Fig. 2. This implies that the modern global Mg cycle is near neutral in dolostone weathering and burial cycles, considering the uncertainty in the models. Therefore, the large difference between $\delta^{26}Mg_{sw}$ at 2 Ga and the modern $\delta^{26}Mg_{sw}$ shows that Earth's surficial Mg cycles varied substantially over geological time.

To quantitatively understand how Earth's surficial Mg cycles evolved through time, we extend the elemental and isotopic mass balance equations to the 2-billion-year record of $\delta^{26}Mg_{sw}$ from this study. For the Monte Carlo calculation, we assume that $F_{carb\text{-}in}/F_{total\text{-}in}$ increased from 0.14 ± 0.04 at 2 Ga to 0.42 ± 0.04 at present or that $F_{carb\text{-}in}/F_{total\text{-}in}$ could be any value between 0 and 1 and calculated the NDB over the past 2 billion years based on the $\delta^{26}Mg_{sw}$ curve using the abovementioned Monte Carlo method. The results not only confirm the decrease in NDB in the Mg cycle over the past 2 billion years but further imply that the decrease is not steady and monotonic (Fig. 3). A notable feature of the NDB trend is the large fluctuation between 330 and 250 Ma. The recognition of such fluctuation is due to higher data density during the Phanerozoic (Fig. 3B). The pattern of the average values of NDB through time is markedly similar to the $\delta^{26}Mg_{sw}$ curve, although the magnitude of the decline in NDB is smaller than that of $\delta^{26}Mg_{sw}$. That is because the lowering of $\delta^{26}Mg_{sw}$ is produced by changes in NDB and by decreasing $\delta^{26}Mg$ of weathered dolostones, which confirms the sensitivity of Mg isotopes in seawater as a tracer of surficial Mg cycles.

DISCUSSION

In the classic view of the silicate-carbonate cycle, if carbonate burial exceeds carbonate weathering, then the excess carbonate burial consumes the alkalinity generated by silicate weathering and consequently removes CO_2 from the Earth's surface (Eq. 3) (*3*).

$$MgSiO_3 + CO_2 \rightarrow MgCO_3 + SiO_2 \quad (3)$$

In light of this, secular changes in NDB for the Earth's surficial Mg cycles have a direct impact on CO_2 removal. An NDB of 0.66 ± 0.19 (2σ) at 2 billion years ago means that, for every 1 mol of Mg cycled on the Paleoproterozoic Earth's surface, 0.66 ± 0.19 (2σ) mol of CO_2 was removed from the atmosphere by the imbalance between dolostone

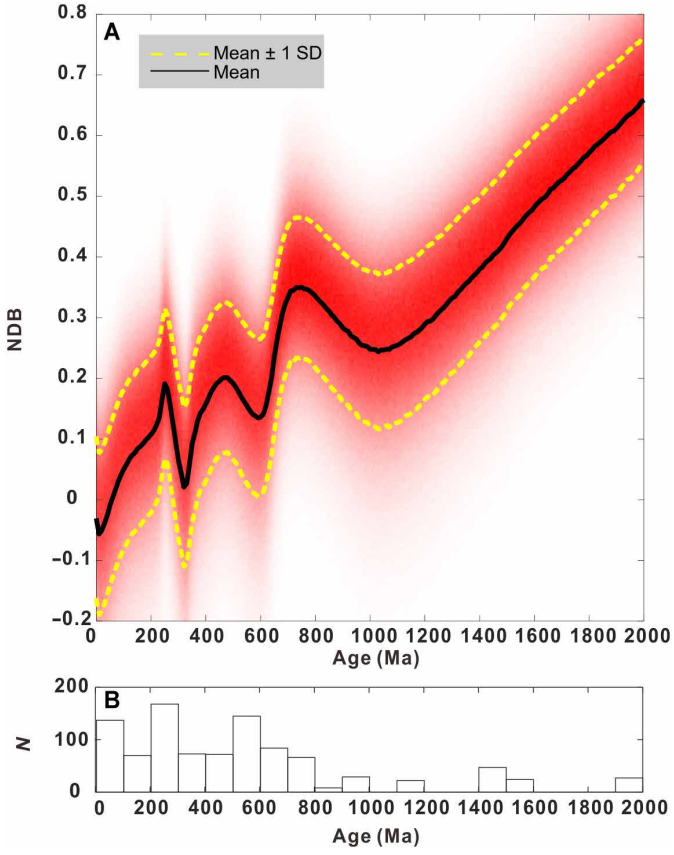

Fig. 3. Monte Carlo modeling results quantitatively reveal how Earth's surficial Mg cycles evolved through time. Evolution of NDB (**A**) and data density (**B**) over the past 2 billion years ($NDB = F_{carb\text{-}out}/F_{total\text{-}out} - F_{carb\text{-}in}/F_{total\text{-}in}$). The black line is the average of Monte Carlo simulation results, and the yellow dashed lines denote the 1sd range of the simulation results.

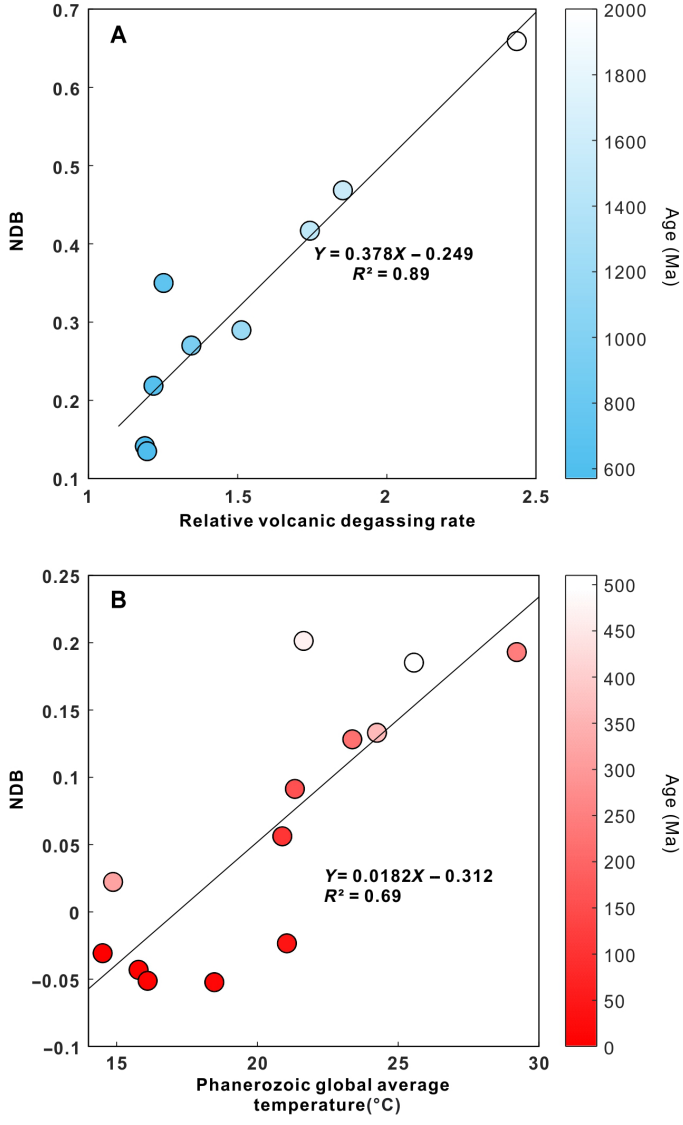

Fig. 4. The linkages between Earth's surficial Mg cycles and C cycles and climate. (**A**) Correlation between relative volcanic degassing rate from 500 to 2000 Ma (*37*) and NDB. (**B**) Correlation between Phanerozoic global average temperature (*38*) and NDB. Modeling results are given for periods with measured dolostone δ^{26}Mg.

weathering and burial. In contrast, because the NDB at present is close to zero, the weathering and burial of Mg-bearing carbonates is balanced. Note that an NDB of zero does not mean that the surficial Mg cycles sequester zero CO_2 from the atmosphere. This is because hydrothermal alteration at mid-ocean ridges results in the removal of seawater Mg^{2+} and the release of Ca^{2+} from the basalts (*3*, *36*), and precipitation of the excess Ca^{2+} from hydrothermal fluids as carbonates removes CO_2. The hydrothermal Mg flux is estimated to be up to 3.1 Tmol/year in the modern oceans, accounting for up to 56% of the total Mg outflux (*8*, *35*). Therefore, presently, the Earth's removal of CO_2 in the surficial Mg cycle is predominantly operated via an indirect route, i.e., through Mg-Ca exchange and subsequent $CaCO_3$ precipitation in the oceans. In contrast, direct dolostone precipitation was a major factor in CO_2 removal for Earth's Mg surficial cycles at 2.0 Ga based on NBD. Therefore, the long-term interplay between Earth's surficial Mg cycles and carbon cycles has evolved over the past 2 billion years.

Studies of the thermal history of Earth's mantle suggest that volcanic degassing declined by twofold from 2000 to 500 Ma (*37*), while our modeling shows that the NDB decreased by a factor of three over the same period (Fig. 4A). This correlation suggests a possible link between NDB and Earth's CO_2 cycles. In light of this, we further explore the response of the NDB to Earth's climate during the Phanerozoic, when Earth's climatic history is relatively well-reconstructed (*38*). As shown in Fig. 4B, in the past 500 Ma, there is a broad positive correlation between NDB and average global temperature. The two correlations in Fig. 4 suggest that NDB responded to, and/or participated in, the regulation of Earth's climate over geological time. Considering the coupling of the Mg and C cycles, as illustrated in Eq. 3, it is possible that NBD has functioned as a geological thermostat.

Phanerozoic global environmental records are compiled in Fig. 5 to explore the NDB geo-thermostat. The NDB curve shows broad correlations (or anticorrelations) with records of continental glaciation, global sea level, and average global surface temperature over the Phanerozoic. When Earth was in ice-house climate states (i.e., low-latitude glaciation, low sea level, and low average temperature), lower sea levels led to the exposure of carbonate platforms which increased

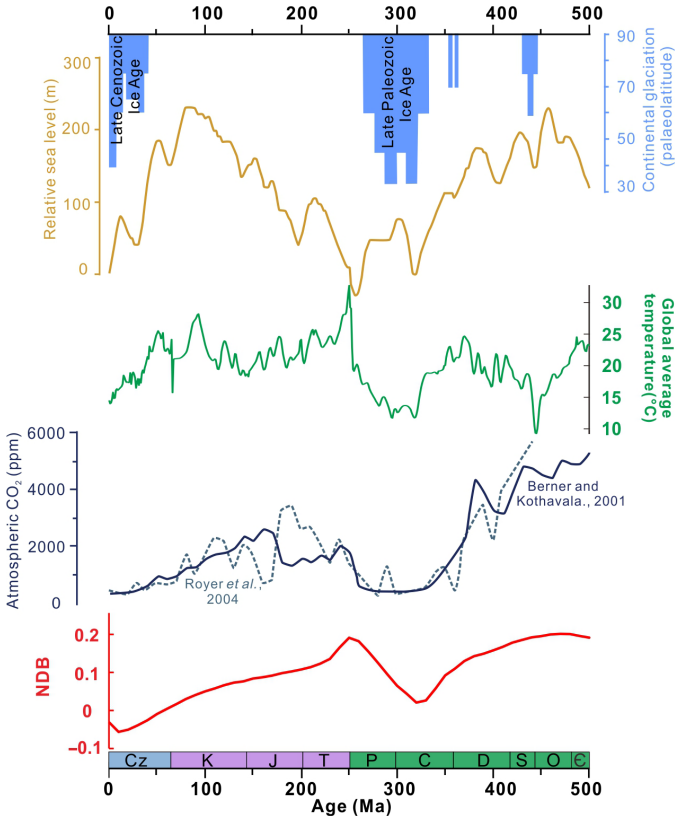

Fig. 5. Comparison of Earth's surficial Mg cycles with other global environmental records. Temporal variations in NDB over the Phanerozoic compared to temporal variations in atmospheric CO_2 concentration (*78*, *79*), average global temperature (*38*), relative sea-level (*80*), and paleo-latitude of continental glaciation (*81*).

carbonate weathering. Since dolomite precipitation is suppressed at lower temperatures (*39*), less Mg was removed by dolomitization in seawater during ice-house climates. These two processes produced the decrease in NDB (i.e., lower $F_{carb\text{-}out}/F_{total\text{-}out}$ but higher $F_{carb\text{-}in}/F_{total\text{-}in}$), which prevented a further decline in atmospheric CO_2 (Fig. 5) and created effective negative feedback to low atmospheric CO_2 levels and low surficial temperatures.

The dolostone weathering-and-burial cycle is not the only component of the Earth's surficial Mg cycle. Another component of the Earth's surficial Mg cycle that has climatic consequences is the Mg-Ca exchange at the mid-ocean ridges with subsequent $CaCO_3$ precipitation (*3*, *36*). In addition, the surficial Ca cycle via Ca-silicate weathering and subsequent Ca carbonate burial is critical in balancing Earth's carbon cycle (*40*). Quantification of the complete surficial Ca cycle in geological history is beyond the scope of this Mg isotope investigation. Nonetheless, the 1:1 molar ratio of Mg:Ca in dolomite stoichiometry means that the changes in NDB reconstructed in this study can be used to understand the portion of the Ca cycle involved in dolomite weathering and burial. Other parts of the surficial Ca cycle, such as limestone weathering and burial, are out of the reach of Mg isotope tracers. However, 60 to 80% of carbonate was buried as dolostone during the Proterozoic (*41*, *42*). For comparison, the fraction of dolostone burial to the total carbonate burial fluctuated markedly between 2 and 90% in the Phanerozoic, with an estimated bulk average of 30 to 50% (*43*–*45*). Therefore, sedimentary records also show that the relative influence of the Mg cycle (compared with the Ca cycle) on atmospheric CO_2 was stronger in the Proterozoic than the Phanerozoic, which is also in accordance with the NDB trend based on Mg isotopes.

Clay formation in marine sediments or "reverse weathering" (*46*, *47*) has been proposed as a geological thermostat (*47*–*49*). It should be noted, however, that such a thermostat mainly functioned during the Precambrian, because the rise of marine siliceous organisms resulted in low Si concentrations in the Phanerozoic oceans (*50*) that suppressed the reverse weathering thermostat (*47*). A recent study suggested that high dissolved Si is favorable for dolomite formation (*51*). Thus, the higher Si content in Precambrian oceans (*50*) may have contributed to the higher proportion of dolostones in Proterozoic carbonate sediments compared to Phanerozoic carbonates. A holistic understanding of the secular evolution of the Earth's atmospheric CO_2 requires quantitative constraints on the surficial cycles of Mg, Ca, and Si. The calculated NDB in the past 2 billion years in this study represents one further step in understanding Earth's long-term surficial cycles.

MATERIALS AND METHODS

Analytical methods

This study performs Mg isotope analysis on halite and dolostone samples. X-ray diffraction analysis of bulk dolostone powder helps screen dolomite-dominated samples for Mg isotope analysis. SEM–energy-dispersive x-ray spectroscopy (EDS) analysis of halite samples is used to identify trace amounts of Mg-bearing evaporite minerals. Sr isotope analysis of halite provides an effective way to identify non-marine signals. All analyses are done at facilities at the State Key Laboratory of Mineral Deposit Research, Nanjing University, China.

Sample preparation

Halite samples are first cleaned by wiping with lint-free paper towels (Kimwipes); about 1- to 2-g sample is scraped off by a tungsten carbide scraper and subsequently ultrasonically cleaned in anhydrous ethanol (>99.7%) for 5 min. After the sample is cleaned and dried, it is dissolved in 12 ml of deionized water (18.2 megohm cm) as a stock solution (*22*, *52*). The dolostone samples are ground into 200 mesh in a precleaned agate mortar. About 10 mg of powder is weighed and dissolved in 5 ml of 1.5 M HAC (CH_3COOH) in a Teflon beaker. Then, the dolostone sample solution is placed on a hotplate (96°C) for about 12 hours for digestion.

Mineral analyses

The mineralogy of the dolostone samples is determined by a Rigaku RAPID II or a Bruker D8 Advance x-ray diffractometer. The Rigaku RAPID II instrument operates at 50 kV and 90 mA on a rotating Mo anode x-ray source; the Bruker D8 Advance instrument runs at 40 kV and 40 mA with a Cu anode x-ray source. X-ray diffraction data processing and mineral identification are performed using Jade 6.5 software. The relative abundance of dolomite (104), calcite (104), and quartz (101) is estimated from the area of characteristic diffraction peaks (*53*). Textural analysis of the halite samples is performed on a Hitachi SU1510 Variable Pressure SEM, and the chemical compositions are characterized using EDS equipped with SEM.

Element analyses

A small fraction of the stock solution from the halite and dolostone samples is extracted and diluted to 4 ml in 2% double-distilled HNO_3. The concentrations of elements (such as Mg, Ca, and Sr) are measured using the inductively coupled plasma optical emission spectrometer (ICP-OES; Skyray ICP-3000). Calibration curves for a series of gravimetrically prepared commercially available multi-element standards with linear correlation coefficients (R^2) are better than 0.999. A 1 parts per million (ppm) multi-element standard is bracketed every 10 samples to monitor and correct the instrument drift. The long-term external accuracy (2RSD, two times relative standard deviation) of elemental analysis is better than 10% (*22*, *52*).

Isotope analyses

Mg isotope analyses

On the basis of the stock solution concentration measured by ICP-OES, an aliquot of the sample containing approximately 20 μg of Mg is used for Mg isotope analysis. To remove sodium, the halite sample is pre-enriched in Mg by precipitation of $Mg(OH)_2$ before undergoing the ion-exchange procedures (*22*). Halite and dolostone samples are further purified by cationic resin (AG50W-X12 and X8) together; see (*21*) for the process. After column chemistry treatments, Mg recovery is better than 95%, and the total matrix elements are less than 1% of Mg.

Mg isotopes are measured on a Thermo Fisher Scientific NEPTUNE Plus multicollector inductively coupled plasma mass spectrometry (MC-ICP-MS) or a Nu 1700 Sapphire MC-ICP-MS. Both instruments operate on a standard low resolution, wet plasma mode. The sample solution is introduced at an uptake rate of 100 μl/min. The method of standard-sample-standard bracketing is used to correct the instrumental drift and mass bias. Each Mg isotope ratio measurement consists of 50 cycles of 4-s integrations. Two pure Mg stock solutions [HPS909104: produced by High Purity Standards Company; A-Mg: prepared by dissolution guaranteed reagent $Mg(NO_3)_2$ solid] serve as in-house bracketing Mg standards. Although there is a difference in the on-machine concentration of pure Mg between the two instruments (Nu 1700: 0.5 ppm; Neptune: 1 ppm), the sample concentration is required to match the standard (the difference less than 10%) in the respective analysis processes. Moreover, the $\delta^{26}Mg$ value of the in-house bracketing Mg standards [$\delta^{26}Mg_{HPS909104} = -0.67 \pm 0.13$‰, $n = 47$, (*54*); $\delta^{26}Mg_{A\text{-}Mg} = -3.25 \pm 0.06$‰, $n = 107$] relative to international standard DSM3 is well-calibrated. Analytical accuracy is monitored by international Mg isotope standards DSM3 and Cambridge1. The International Association for the Physical Sciences of the Oceans (IAPSO) seawater and United States Geological Survey (USGS) rock (DTS-2) standards are processed along with samples to verify the accuracy of chemical procedures. The measured $\delta^{26}Mg$ values of the standards (table S4) match the published values (*13*, *54*), and the long-term external analytical precision was better than ±0.1‰.

Sr isotope analyses

An aliquot of the halite stock solution containing approximately 500 ng Sr is extracted for Sr isotope analyses. The Sr-spec resin is used to purify the sample (*55*). The sample is loaded in 3 N HNO_3, and Sr is collected with 0.05 N HNO_3. The USGS rock (AGV-2) and IAPSO seawater standards are treated as unknown samples to monitor the analysis procedure. Strontium isotope analysis is performed using a Finnigan Triton thermal ionization mass spectrometer. At the beginning of every analytical sequence, the international standard NIST 987 ($^{87}Sr/^{86}Sr = 0.710228 \pm 0.000033$, $2\sigma = 100$) is measured to verify the instrument status. With exponential law, the Sr isotope data are normalized to $^{86}Sr/^{88}Sr = 0.1194$. All the measured $^{87}Sr/^{86}Sr$ ratios of standards (table S4) are consistent with published values (*21*, *52*, *56*).

Isotopic mass balance model based on a Monte Carlo approach

The model framework

The primary sources of Mg in the ocean include silicate weathering and carbonate weathering. The major outputs are dolomitization, low-temperature and high-temperature alteration of basalt, and authigenic clay formation (*8*). For simplification, we use a single symbol sil-out to represent all the processes that uptake Mg from seawater into silicate minerals, including low-temperature and high-temperature alteration of basalt and authigenic clay formation. Similarly, carb-out, carb-in, and sil-in represent dolomitization, carbonate weathering, and silicate weathering, respectively. By assuming that the Mg cycle is at steady state [a treatment that has been universally applied in relevant studies for Li (*33*, *57*), Mg (*8*, *35*, *58*), K (*59*, *60*), Mo (*61*–*63*), and U (*64*–*67*)], we have

$$F_{\text{carb-in}} + F_{\text{sili-in}} = F_{\text{carb-out}} + F_{\text{sili-out}} \quad (4)$$

$$\delta_{\text{carb-in}}F_{\text{carb-in}} + \delta_{\text{sili-in}}F_{\text{sili-in}} = \delta_{\text{carb-out}}F_{\text{carb-out}} + \delta_{\text{sili-out}}F_{\text{sili-out}} \quad (5)$$

where F represents the Mg fluxes and δ stands for isotopic compositions of the Mg flux for the major components that participate in the Mg cycle.

Then, for ease of programming, we divide the two sides of the equation by the total flux that goes into the ocean (i.e., $F_{\text{carb-in}} + F_{\text{sili-in}}$) and let $f_{\text{carb-in}}$ represent the fraction of the Mg flux derived from carbonate weathering in the total Mg input flux, and $f_{\text{carb-out}}$ stands for the fraction of Mg in seawater deposited as carbonates. The two equations can be simplified to

$$\begin{aligned}&\delta_{\text{carb-in}}f_{\text{carb-in}} + \delta_{\text{sili-in}}(1 - f_{\text{carb-in}}) = \\ &\delta_{\text{carb-out}}f_{\text{carb-out}} + \delta_{\text{sili-out}}(1 - f_{\text{carb-out}})\end{aligned} \quad (6)$$

Here, $\delta_{\text{carb-out}}$ and $\delta_{\text{sili-out}}$ are functions of the Mg isotopic composition of seawater (δ_{sw})

$$\delta_{\text{carb-out}} = \delta_{sw} + \Delta_{\text{carb-out}} \quad (7)$$

$$\delta_{\text{sili-out}} = \delta_{sw} + \Delta_{\text{sil-out}} \quad (8)$$

With Eqs. 6 to 8, we built a model that calculates how the Mg cycle evolves with the record of the Mg isotopic composition of seawater.

Model parameters

In this section, we describe how we quantify the model parameters. Considering that Mg, sourced from carbonate weathering ($F_{\text{carb-in}}$), is dominated by dolomite (*68*), and in the long-run, dolomite weathering is congruent, $\delta_{\text{carb-in}}$ is set to be the weighted average of $\delta^{26}Mg$ of the previously deposited dolostones, which are compiled in Fig. 1 of the main text. The fraction of dolostone that remains on the continent (R) is estimated from a time-dependent decay function following (*11*)

$$R = e^{-0.001T} \quad (9)$$

Here, T (in Ma) is the time elapsed since the deposition of dolostone. The δ^{26}Mg of the dolostone is calculated from the Mg isotopic composition of seawater by assuming a fractionation factor of -1.5 ± 0.2‰ (1 SD). Then, $\delta_{carb\text{-}in}$ is determined as the R-weighted average of δ^{26}Mg of the weathered dolostones; calculation results are shown in fig. S11A. Considering that silicate weathering is associated with clay formation that generally enriches heavy Mg isotopes, $\delta_{sili\text{-}in}$ is assumed to be close to, but slightly lighter than, the δ^{26}Mg of the bulk silicate earth (*13*), with a value of -0.4 ± 0.1 ‰ (1 SD). For the calculation of $\delta_{carb\text{-}out}$ with Eq. 7, $\Delta_{carb\text{-}out}$ is estimated to be ~−1.5‰ with 1 SD of 0.2‰ (*16*). The fractionation involved in the alteration of seafloor basalt and formation of authigenic marine clays varies substantially, ranging from 0 to 1.6‰ (*17*, *35*). To cover this range and account for uncertainty, we assume that $\Delta_{sil\text{-}out}$ is 0.8 ± 0.4‰ (1 SD).

The quantification of $f_{carb\text{-}in}$ is more complicated. In the modern world, estimates of the fraction of Mg flux derived from silicate weathering vary considerably, ranging from 0.48 to 0.59 (*8*, *40*, *68*, *69*). Accordingly, $f_{carb\text{-}in}$ ranges from 0.41 to 0.52. Another factor that affects the quantification of $f_{carb\text{-}in}$ is marine silicate weathering, which has drawn increasing attention recently (*70*–*72*). On the basis of a methane generation estimate ranging from 7 to 300×10^{12} mol/year (*73*, *74*), Wallmann *et al.* (*72*) estimated that the CO_2 consumption rate by marine silicate weathering is 5 to 20×10^{12} mol/year. Using an updated methane generation flux of $\sim 1.2 \times 10^{12}$ mol/year (*75*), the estimate of marine silicate weathering is revised to 1 to 4×10^{12} mol/year (*71*). The latter is close to the estimate of 1×10^{12}mol/year by (*76*) based on the global authigenic Ca carbonate flux. Therefore, in this study, we use 1 to 4×10^{12} mol/year as the best estimate of the global marine silicate weathering rate, which is 8.5 to 34.1% of the subaerial silicate weathering rate (*77*). Assuming silicate weathering follows the same stoichiometries in both terrestrial and marine environments, $f_{carb\text{-}in}$ ranges from 0.34 to 0.50 if we consider the marine silicate weathering flux. In other words, a $f_{carb\text{-}in}$ value of 0.42 ± 0.04 (1 SD) is used for the modern.

During Earth's history earlier than 3 Ga, $f_{carb\text{-}in}$ is assumed to be 0 because carbonates cannot be exposed to weathering without tectonic uplift (*73*, *74*). For any time between 0 and 3 Ga, we assume that $f_{carb\text{-}in}$ increased from 0 to the modern value, with an SD of 0.1. In other words, if t represents age (in Ma), we have

$$f_{carb\text{-}in} = 0.42 \; - \; 0.42 \; * \; t \,/\, 3000 \qquad (10)$$

The curve of $f_{carb\text{-}in}$ is presented in fig. S11B. For δ_{sw} at a specific time, we estimate the δ_{sw} value with linear interpolation, assuming that the δ_{sw} record has a 1 SD uncertainty of 0.1 (fig. S11C).

Supplementary Materials

This PDF file includes:

Supplementary Text
Figs. S1 to S15
Tables S1 to S4
Legends for data files S1 and S2

Other Supplementary Material for this manuscript includes the following:

Data files S1 and S2
Auxiliary References

REFERENCES AND NOTES

1. L. R. Kump, S. L. Brantley, M. A. Arthur, Chemical Weathering, Atmospheric CO_2, and Climate. *Annu. Rev. Earth Planet. Sci.* **28**, 611–667 (2000).
2. J. C. G. Walker, P. B. Hays, J. F. Kasting, A negative feedback mechanism for the long-term stabilization of Earth's surface temperature. *J. Geophys. Res. Oceans* **86**, 9776–9782 (1981).
3. R. Berner, A. Lasaga, R. Garrells, The carbonate-silicate geochemical cycle and its effect on atmospheric carbon dioxide over the past 100 million years. *Am. J. Sci.* **283**, 641–683 (1983).
4. G. Li, J. Hartmann, L. A. Derry, A. J. West, C.-F. You, X. Long, T. Zhan, L. Li, G. Li, W. Qiu, T. Li, L. Liu, Y. Chen, J. Ji, L. Zhao, J. Chen, Temperature dependence of basalt weathering. *Earth Planet. Sci. Lett.* **443**, 59–69 (2016).
5. L. François, J. Walker, Modelling the Phanerozoic carbon cycle and climate: Constraints from the $^{87}Sr/^{86}Sr$ isotopic ratio of seawater. *Am. J. Sci.* **292**, 81–135 (1992).
6. H. Staudigel, S. R. Hart, H.-U. Schmincke, B. M. Smith, Cretaceous ocean crust at DSDP Sites 417 and 418: Carbon uptake from weathering versus loss by magmatic outgassing. *Geochim. Cosmochim. Acta* **53**, 3091–3094 (1989).
7. A. G. Dunlea, R. W. Murray, D. P. Santiago Ramos, J. A. Higgins, Cenozoic global cooling and increased seawater Mg/Ca via reduced reverse weathering. *Nat. Commun.* **8**, 844 (2017).
8. J. A. Higgins, D. P. Schrag, The Mg isotopic composition of Cenozoic seawater – evidence for a link between Mg-clays, seawater Mg/Ca, and climate. *Earth Planet. Sci. Lett.* **416**, 73–81 (2015).
9. B. H. Wilkinson, T. J. Algeo, Sedimentary carbonate record of calcium-magnesium cycling. *Am. J. Sci.* **289**, 1158–1194 (1989).
10. R. Berner, A model for calcium, magnesium and sulfate in seawater over Phanerozoic time. *Am. J. Sci.* **304**, 438–453 (2004).
11. S. E. Peters, J. M. Husson, Sediment cycling on continental and oceanic crust. *Geology* **45**, 323–326 (2017).
12. T. K. Lowenstein, M. N. Timiifeeff, S. T. Brennan, L. A. Hardie, R. V. Demicco, Oscillations in Phanerozoic seawater chemistry: Evidence from fluid inclusions. *Science* **294**, 1086–1088 (2001).
13. F.-Z. Teng, Magnesium Isotope Geochemistry. *Rev. Mineral. Geochem.* **82**, 219–287 (2017).
14. E. Tipper, A. Galy, J. Gaillardet, M. Bickle, H. Elderfield, E. Carder, The magnesium isotope budget of the modern ocean: Constraints from riverine magnesium isotope ratios. *Earth Planet. Sci. Lett.* **250**, 241–253 (2006).
15. D. Alderton, "Carbonates (Ca, Mg, Fe, Mn)" in Encyclopedia of Geology (Second Edition), D. Alderton, S. A. Elias, Eds. (Academic Press, Oxford, 2021), pp. 382–394.
16. W. Li, B. L. Beard, C. Li, H. Xu, C. M. Johnson, Experimental calibration of Mg isotope fractionation between dolomite and aqueous solution and its geological implications. *Geochim. Cosmochim. Acta* **157**, 164–181 (2015).
17. J. A. Higgins, D. P. Schrag, Constraining magnesium cycling in marine sediments using magnesium isotopes. *Geochim. Cosmochim. Acta* **74**, 5039–5053 (2010).
18. A. M. Gothmann, J. Stolarski, J. F. Adkins, J. A. Higgins, A Cenozoic record of seawater Mg isotopes in well-preserved fossil corals. *Geology* **45**, 1039–1042 (2017).
19. R. N. Bryant, T. M. Present, A.-S. C. Ahm, H.-L. O. McClelland, D. Razionale, C. L. Blättler, Early diagenetic constraints on Permian seawater chemistry from the Capitan Reef. *Geochim. Cosmochim. Acta* **328**, 1–18 (2022).
20. A. Geske, J. Zorlu, D. K. Richter, D. Buhl, A. Niedermayr, A. Immenhauser, Impact of diagenesis and low grade metamorphosis on isotope (δ^{26}Mg, δ^{13}C, δ^{18}O and $^{87}Sr/^{86}Sr$) and elemental (Ca, Mg, Mn, Fe and Sr) signatures of Triassic sabkha dolomites. *Chem. Geol.* **332-333**, 45–64 (2012).
21. Z. Hu, W. Hu, X. Wang, Y. Lu, L. Wang, Z. Liao, W. Li, Resetting of Mg isotopes between calcite and dolomite during burial metamorphism: Outlook of Mg isotopes as geothermometer and seawater proxy. *Geochim. Cosmochim. Acta* **208**, 24–40 (2017).
22. Z. Xia, J. Horita, L. Reuning, O. M. Bialik, Z. Hu, N. D. Waldmann, C. Liu, W. Li, Extracting Mg isotope signatures of ancient seawater from marine halite: A reconnaissance. *Chem. Geol.* **552**, 119768 (2020).
23. A. Geske, R. Goldstein, V. Mavromatis, D. K. Richter, D. Buhl, T. Kluge, C. John, A. Immenhauser, The magnesium isotope (δ^{26}Mg) signature of dolomites. *Geochim. Cosmochim. Acta* **149**, 131–151 (2015).
24. N. Shalev, T. R. R. Bontognali, D. Vance, Sabkha dolomite as an archive for the magnesium isotope composition of seawater. *Geology* **49**, 253–257 (2021).
25. M. Ning, X. Lang, K. Huang, C. Li, T. Huang, H. Yuan, C. Xing, R. Yang, B. Shen, Towards understanding the origin of massive dolostones. *Earth Planet. Sci. Lett.* **545**, 116403 (2020).
26. M. S. Fantle, J. Higgins, The effects of diagenesis and dolomitization on Ca and Mg isotopes in marine platform carbonates: Implications for the geochemical cycles of Ca and Mg. *Geochim. Cosmochim. Acta* **142**, 458–481 (2014).
27. Z. Hu, W. Li, H. Zhang, K. Krainer, Q.-f. Zheng, Z. Xia, W. Hu, S.-z. Shen, Mg isotope evidence for restriction events within the Paleotethys ocean around the Permian-Triassic transition. *Earth Planet. Sci. Lett.* **556**, 116704 (2021).

28. O. M. Bialik, X. Wang, S. Zhao, N. D. Waldmann, R. Frank, W. Li, Mg isotope response to dolomitization in hinterland-attached carbonate platforms: Outlook of δ^{26}Mg as a tracer of basin restriction and seawater Mg/Ca ratio. *Geochim. Cosmochim. Acta* **235**, 189–207 (2018).
29. P. F. Hoffman, A. J. Kaufman, G. P. Halverson, D. P. Schrag, A Neoproterozoic Snowball Earth. *Science* **281**, 1342–1346 (1998).
30. T. W. Lyons, C. W. Diamond, N. J. Planavsky, C. T. Reinhard, C. Li, Oxygenation, life, and the planetary system during Earth's middle history: An overview. *Astrobiology* **21**, 906–923 (2021).
31. M. Tang, X. Chu, J. Hao, B. Shen, Orogenic quiescence in Earth's middle age. *Science* **371**, 728–731 (2021).
32. H. Elderfield, A. Schultz, Mid-Ocean Ridge Hydrothermal Fluxes and the Chemical Composition of the Ocean. *Annu. Rev. Earth Planet. Sci.* **24**, 191–224 (1996).
33. B. Kalderon-Asael, J. A. R. Katchinoff, N. J. Planavsky, A. V. S. Hood, M. Dellinger, E. J. Bellefroid, D. S. Jones, A. Hofmann, F. O. Ossa, F. A. Macdonald, C. Wang, T. T. Isson, J. G. Murphy, J. A. Higgins, A. J. West, M. W. Wallace, D. Asael, P. A. E. P. von Strandmann, A lithium-isotope perspective on the evolution of carbon and silicon cycles. *Nature* **595**, 394–398 (2021).
34. G. Li, A. J. West, Evolution of Cenozoic seawater lithium isotopes: Coupling of global denudation regime and shifting seawater sinks. *Earth Planet. Sci. Lett.* **401**, 284–293 (2014).
35. N. Shalev, T. Bontognali, C. G. Wheat, D. Vance, New isotope constraints on the Mg oceanic budget point to cryptic modern dolomite formation. *Nat. Commun.* **10**, 5646 (2019).
36. L. A. Coogan, K. M. Gillis, Low-Temperature Alteration of the Seafloor: Impacts on Ocean Chemistry. *Annu. Rev. Earth Planet. Sci.* **46**, 21–45 (2018).
37. J. B. D. Jaffrés, G. A. Shields, K. Wallmann, The oxygen isotope evolution of seawater: A critical review of a long-standing controversy and an improved geological water cycle model for the past 3.4 billion years. *Earth Sci. Rev.* **83**, 83–122 (2007).
38. C. R. Scotese, H. Song, B. J. W. Mills, D. G. van der Meer, Phanerozoic paleotemperatures: The earth's changing climate during the last 540 million years. *Earth Sci. Rev.* **215**, 103503 (2021).
39. S. E. Kaczmarek, B. P. Thornton, The effect of temperature on stoichiometry, cation ordering, and reaction rate in high-temperature dolomitization experiments. *Chem. Geol.* **468**, 32–41 (2017).
40. E. K. Berner, R. A. Berner, *Global Environment: Water Air and Geochemical Cycles* (Prentice-Hall, 1996), vol. 60.
41. I. Halevy, A. Bachan, The geologic history of seawater pH. *Science* **355**, 1069–1071 (2017).
42. M. D. Cantine, A. H. Knoll, K. D. Bergmann, Carbonates before skeletons: A database approach. *Earth Sci. Rev.* **201**, 103065 (2020).
43. R. K. Given, B. H. Wilkinson, Dolomite abundance and stratigraphic age; constraints on rates and mechanisms of Phanerozoic dolostone formation. *J. Sediment. Res.* **57**, 1068–1078 (1987).
44. M. Li, P. B. Wignall, X. Dai, M. Hu, H. Song, Phanerozoic variation in dolomite abundance linked to oceanic anoxia. *Geology* **49**, 698–702 (2021).
45. J. M. Husson, L. A. Coogan, River chemistry reveals a large decrease in dolomite abundance across the Phanerozoic. *Geochem. Perspect. Lett.* **26**, 1–6 (2023).
46. P. Michalopoulos, R. C. Aller, Rapid clay mineral formation in Amazon delta Sediments: Reverse Weathering and Oceanic Elemental Cycles. *Science* **270**, 614–617 (1995).
47. T. T. Isson, N. J. Planavsky, Reverse weathering as a long-term stabilizer of marine pH and planetary climate. *Nature* **560**, 471–475 (2018).
48. J. Ma, X. Shi, M. Lechte, X. Zhou, Z. Wang, K. Huang, M. Rudmin, D. Tang, Mesoproterozoic seafloor authigenic glauconite-berthierine: Indicator of enhanced reverse weathering on early Earth. *Am. Mineral.* **107**, 116–130 (2022).
49. E. Trower, W. Fischer, Precambrian Si isotope mass balance, weathering, and the significance of the authigenic clay silica sink. *Sediment. Geol.* **384**, 1–11 (2019).
50. D. J. Conley, P. J. Frings, G. Fontorbe, W. Clymans, J. Stadmark, K. R. Hendry, A. O. Marron, C. L. De La Rocha, Biosilicification drives a decline of dissolved Si in the oceans through geologic time. *Front. Mar. Sci.* **4**, (2017).
51. Y. Fang, F. Hobbs, Y. Yang, H. Xu, Dissolved silica-driven dolomite precipitation in the Great Salt Lake, Utah, and its implication for dolomite formation environments. *Sedimentology* **70**, 1328–1347 (2023).
52. Z. Xia, Y. Lin, H. Wei, Z. Hu, C. Liu, W. Li, Reconstruct hydrological history of terrestrial saline lakes using Mg isotopes in halite: A case study of the Quaternary Dalangtan playa in Qaidam Basin, NW China. *Palaeogeogr. Palaeoclimatol. Palaeoecol.* **587**, 110804 (2022).
53. L. S. Zevin, A method of quantitative phase analysis without standards. *J. Appl. Cryst.* **10**, 147–150 (1977).
54. W. Li, S. Chakraborty, B. L. Beard, C. S. Romanek, C. M. Johnson, Magnesium isotope fractionation during precipitation of inorganic calcite under laboratory conditions. *Earth Planet. Sci. Lett.* **333-334**, 304–316 (2012).
55. D. De Muynck, G. Huelga-Suarez, L. Van Heghe, P. Degryse, F. Vanhaecke, Systematic evaluation of a strontium-specific extraction chromatographic resin for obtaining a purified Sr fraction with quantitative recovery from complex and Ca-rich matrices. *J. Anal. At. Spectrom* **24**, 1498–1510 (2009).
56. G. Wei, J. Ma, Y. Liu, L. Xie, W. Lu, W. Deng, Z. Ren, T. Zeng, Y. Yang, Seasonal changes in the radiogenic and stable strontium isotopic composition of Xijiang River water: Implications for chemical weathering. *Chem. Geol.* **343**, 67–75 (2013).
57. S. Misra, P. N. Froelich, Lithium isotope history of Cenozoic seawater: Changes in silicate weathering and reverse weathering. *Science* **335**, 818–823 (2012).
58. R. Berg, E. Solomon, F.-Z. Teng, The role of marine sediment diagenesis in the modern oceanic magnesium cycle. *Nat. Commun.* **10**, 4371 (2019).
59. Y. Hu, F.-Z. Teng, T. Plank, C. Chauvel, Potassium isotopic heterogeneity in subducting oceanic plates. *Sci. Adv.* **6**, eabb2472 (2020).
60. S. Li, W. Li, B. L. Beard, M. E. Raymo, X. Wang, Y. Chen, J. Chen, K isotopes as a tracer for continental weathering and geological K cycling. *Proc. Natl. Acad. Sci. U.S.A.* **116**, 8740–8745 (2019).
61. C. Archer, D. Vance, The isotopic signature of the global riverine molybdenum flux and anoxia in the ancient oceans. *Nat. Geosci.* **1**, 597–600 (2008).
62. G. L. Arnold, A. D. Anbar, J. Barling, T. W. Lyons, Molybdenum isotope evidence for widespread anoxia in mid-Proterozoic oceans. *Science* **304**, 87–90 (2004).
63. A. J. Dickson, A molybdenum-isotope perspective on Phanerozoic deoxygenation events. *Nat. Geosci.* **10**, 721–726 (2017).
64. R. Bartlett, M. Elrick, R. Wheeley James, V. Polyak, A. Desrochers, Y. Asmerom, Abrupt global-ocean anoxia during the Late Ordovician–early Silurian detected using uranium isotopes of marine carbonates. *Proc. Natl. Acad. Sci. U.S.A.* **115**, 5896–5901 (2018).
65. A. Brennecka Gregory, D. Herrmann Achim, J. Algeo Thomas, D. Anbar Ariel, Rapid expansion of oceanic anoxia immediately before the end-Permian mass extinction. *Proc. Natl. Acad. Sci. U.S.A.* **108**, 17631–17634 (2011).
66. M. O. Clarkson, T. M. Lenton, M. B. Andersen, M.-L. Bagard, A. J. Dickson, D. Vance, Upper limits on the extent of seafloor anoxia during the PETM from uranium isotopes. *Nat. Commun.* **12**, 399 (2021).
67. F. Zhang, S. Xiao, B. Kendall, J. Romaniello Stephen, H. Cui, M. Meyer, J. Gilleaudeau Geoffrey, J. Kaufman Alan, A. D. Anbar, Extensive marine anoxia during the terminal Ediacaran Period. *Sci. Adv.* **4**, eaan8983 (2018).
68. M. Meybeck, Global chemical weathering of surficial rocks estimated from river dissolved loads. *Am. J. Sci.* **287**, 401–428 (1987).
69. T. Zhao, W. Liu, Z. Xu, Magnesium isotope fractionation during silicate weathering: Constrains from riverine Mg isotopic composition in the Southeastern Coastal Region of China. *Geochem. Geophys. Geosyst.* **23**, e2021GC010100 (2022).
70. J.-H. Kim, M. E. Torres, B. A. Haley, J.-S. Ryu, M.-H. Park, W.-L. Hong, J. Choi, Marine silicate weathering in the anoxic sediment of the Ulleung Basin: Evidence and consequences. *Geochem. Geophys. Geosyst.* **17**, 3437–3453 (2016).
71. M. E. Torres, W.-L. Hong, E. A. Solomon, K. Milliken, J.-H. Kim, J. C. Sample, B. M. A. Teichert, K. Wallmann, Silicate weathering in anoxic marine sediment as a requirement for authigenic carbonate burial. *Earth Sci. Rev.* **200**, 102960 (2020).
72. K. Wallmann, G. Aloisi, M. Haeckel, P. Tishchenko, G. Pavlova, J. Greinert, S. Kutterolf, A. Eisenhauer, Silicate weathering in anoxic marine sediments. *Geochim. Cosmochim. Acta* **72**, 2895–2918 (2008).
73. K. U. Hinrichs, A. Boetius, "The Anaerobic Oxidation of Methane: New Insights in Microbial Ecology and Biogeochemistry" in Ocean Margin Systems, G. Wefer, D. Billett, D. Hebbeln, B. B. Jørgensen, M. Schlüter, T. C. E. van Weering, Eds. (Springer Berlin Heidelberg, Berlin, Heidelberg, 2002), pp. 457–477.
74. W. Reeburgh, S. Whalen, M. Alperin, The role of methylotrophy in the global methane budget. Microbial Growth on C Compounds, 1-14 (1993).
75. K. Wallmann, E. Pinero, E. Burwicz, M. Haeckel, C. Hensen, A. Dale, L. Ruepke, The Global Inventory of Methane Hydrate in Marine Sediments: A Theoretical Approach. *Energies* **5**, 2449–2498 (2012).
76. X. Sun, A. V. Turchyn, Significant contribution of authigenic carbonate to marine carbon burial. *Nat. Geosci.* **7**, 201–204 (2014).
77. J. Gaillardet, B. Dupré, P. Louvat, C. J. Allègre, Global silicate weathering and CO_2 consumption rates deduced from the chemistry of large rivers. *Chem. Geol.* **159**, 3–30 (1999).
78. R. Royer, I. Berner, N. Montañez, D. Tabor, CO_2 as a primary driver of Phanerozoic climate. *GSA Today* **14**, 3–7 (2004).
79. R. A. Berner, Z. Kothavala, Geocarb III: A revised model of atmospheric CO_2 over Phanerozoic time. *Am. J. Sci.* **301**, 182–204 (2001).
80. U. Haq Bilal, R. Schutter Stephen, A chronology of Paleozoic sea-level changes. *Science* **322**, 64–68 (2008).
81. T. J. Crowley, *Significance of tectonic boundary conditions for paleoclimate simulations* (Tectonic Boundary Conditions for Climate Reconstructions, Oxford University Press, New York, 1998).

Acknowledgments: We are grateful to C. Wu, X. Wang, X. Chu, L. Gao, Y. Zhang, G. Luo, J. Horita, Y. Kubo, L. Reuning, J. Li, Z. Han, L. Wang, H. Tang, J. Li, Y. Song, X. Wang, and Y. Huang for providing samples or assisting with sampling. M. Palmer provided critical reviews of the manuscript which are highly appreciated. **Funding:** This study is supported by the National Natural Science Foundation of China (92358301 to T.C., 42293280 to S.S., 41991321 to S.L., and 41873004 to W.L.), the Strategic Priority Research Program (B) of the Chinese Academy of Sciences (XDB26020101 to W. L.). F.Z. acknowledges financial support from the National Key

Research and Development Program of China (2021YFA0718100). W.L. was additionally supported by the Research Funds for the Frontiers Science Center for Critical Earth Material Cycling, Nanjing University. **Author contributions:** Conceptualization: W.L., T.K.L., and S.S. Methodology: W.L., Z.X., S.L., S.A., T.K.L., and M.F.W. Investigation: Z.X., O.B., Z.H., M.F.W., X.W., J.C., Z.J., H.X., Q.F., T.C., F.Z., J.F., S.L., T.K.L., W.L., and S.S. Visualization: Z.X., S.L., and O.B. Supervision: W.L., T.K.L., J.F., X.W., and S.S. Writing—original draft: W.L., Z.X., S.L., and T.K.L. Writing—review and editing: W.L., T.K.L., S.L., Z.X., O.B., Z.H., M.F.W., X.W., Q.F., F.Z., J.F., and S.S. Resources: W.L., T.K.L., Z.H., O.B., Q.F., X.W., J.F., and S.S. Data curation: Z.X., S.L., and J.F. Validation: Z.H., O.B., M.F.W., T.C., Q.F., J.C., Z.J., and H.X. Formal analysis: W.L., Z.X., S.L., T.K.L., O.B., Z.H., and S.S. Funding acquisition: W.L., S.S., T.C., and S.L. Software: S.L. and W.L. Project administration: W.L., J.F., and S.S. **Competing interests:** The authors declare that they have no competing interests. **Data and materials availability:** All data needed to evaluate the conclusions in the paper are present in the paper and/or the Supplementary Materials. All model codes are archived at doi.org/10.6084/m9.figshare.24892989.

Submitted 3 July 2023
Accepted 26 January 2024
Published 1 March 2024
10.1126/sciadv.adj5474